Control Choices to Allow the Parallel Operation of Grid-Forming Type-III Wind Turbines

Adrián González-Cajigas , *Student Member, IEEE*, Emilio J. Bueno , *Senior Member, IEEE*,
Javier Roldán-Pérez , *Member, IEEE*, Roberto Martín-López, and Elena Sáiz-Marín

Abstract—**Grid codes are now requesting grid forming capability to renewable energy sources. The provision of this service is being thoroughly investigated for type-IV wind turbines (full electronic interface) with the virtual synchronous machine (VSM) control technique. However, this issue has been barely addressed for type-III wind turbines. In this turbine topology, it is of special interest to keep the current controller of the rotor-side converter (RSC) unaltered since many functions that are required for the safe operation of the machine and to comply with grid codes depend on it. In this article, two control alternatives to implement a VSM without modifying the structure of the inner current controller of type-III wind turbines are proposed. The first one is based on a current controller plus a novel flux-based virtual inductance, while the second one has a more traditional structure based on a current controller, a voltage controller, and a virtual impedance. Results show that a vector voltage controller is not an essential requirement to provide grid-forming capability. In addition, the operation of a wind farm consisting of six parallel-connected type-III wind turbines is studied analytically for both alternatives. The parallel operation of the wind turbines is verified by using real-time simulations performed in OPAL-RT. Finally, the control alternatives were experimentally validated in a real doubly fed induction generator rated at 28 kVA.**

Index Terms—**Island operation, type-III wind turbine, virtual impedance, virtual synchronous machine (VSM), voltage controller.**

I. INTRODUCTION

A. Motivation

IN RECENT years, wind power generation has experienced a great growth and has become one of the most important power resources in the world. However, the massive integration of wind energy plants is leading to significant side effects related to stability and interaction among generators. To cope with the increasing number of interactions, transmission system operators are requesting grid-forming capability and advance control features to renewable generators [1]. Photovoltaic generators have a very limited capacity to inject additional active power since they do not have energy storage elements [2]. On the contrary, wind generators are more suitable for this, since they have kinetic energy stored in their shafts [3]. Type-III wind turbines represent a significant portion of wind power generation. Even though the electrical machine is far more complex than in other alternatives, the power converters are smaller and, therefore, their cost and efficiency are higher [4]. However, grid-forming controllers are different compared with those in which the output is purely electronic. This increases the complexity of the grid-forming control strategy [5]. In type-III wind turbines, it is of interest to keep the inner current control unaltered when implementing grid-forming features. This facilitates to comply with the rest of grid-code requirements. This field has not been studied in depth and it is of interest from both the scientific and industrial points of view.

B. Literature Review

The virtual synchronous machine (VSM) control technique was developed many years ago and was well known in the microgrid community [6]. However, it has now emerged as a relevant candidate for the seamless integration of renewables in power systems [7]. With this control technique, the converter emulates the main characteristics of traditional synchronous generators. Therefore, the renewable generator can work either connected or disconnected from the main grid without substantial modifications in the control system [8].

The VSM control technique has been thoroughly studied in literature [9]. Many of these works focus on the selection of the VSM control parameters [10], [11], [12] while some others propose modifications to the fundamental structure of the VSM to improve the transient response [13]. Many stability analyses have been carried out, mainly by using small-signal analysis techniques [14], [15]. The vast majority of these works is focused on full-electronic interfaces. This means that it can be applied, among others, to photovoltaic generators and type-IV wind turbines. The implementation of the VSM control technique for type-III wind turbines has substantial differences compared with the standard VSM and has been less studied in the literature. As the main difference, the grid interface is not purely electronic

Adrián González-Cajigas, Emilio J. Bueno, and Roberto Martín-López are with Alcalá de Henares Universirty, 28801 Madrid, Spain (e-mail: adrian.gonzalezc@uah.es; emilio.bueno@uah.es; roberto.martin@edu.uah.es).

Javier Roldán-Pérez is with IMDEA Energy, 28935 Madrid, Spain (e-mail: javier.roldan@imdea.org).

Elena Sáiz-Marín is with Siemens Gamesa, 28043 Madrid, Spain (e-mail: elena.saiz@siemensgamesa.com).

and the grid "sees" an equivalent system that is a mix between a machine and a power converter. Therefore, the VSM controller has to be adapted accordingly. In particular, Wang et al. [5] presented a VSM control for doubly fed induction generators (DFIGs) and compare it with an inertial control implemented on top of a vector control. The results show that the VSM alternative presents better stability margins in weak grids and provides a better frequency support. Shao et al. [16] proposed a combination of a VSM for the rotor-side converter (RSC) and an inertial control for the grid-side converter (GSC). The controller is compared with other ones, and it is shown that it has a better transient response. However, neither of these alternatives include an internal current controller. The absence of this loop represents an important limitation to guarantee the safe operation of the wind turbine during transient events. Grid codes usually request the injection of specific current and/or power profiles during these events, and the VSM without internal current controllers is not well suited for this [17]. This is particularly relevant for DFIGs, as they are very sensitive to grid disturbances [18]. For this reason, the VSM has to be replaced by a regular vector current control (grid-following mode) in these cases [19], [20]. A method to avoid switching between grid-forming and grid-following control modes is to use a virtual resistance. In this case, the current flowing through the converter is limited by emulating a resistance with the control system. In [21], a virtual resistance is proposed to reduce the current during transients while keeping the reactive power injection constant. Nian Jiao [22] proposed a VSM controller for improving the response of a DFIG in these scenarios. The solution comes in the form of feedforward terms and a virtual resistance that speeds up the decay of transient components and limits the rotor current. The same issue is addressed by Wang et al. [23], where adaptive feedforward terms are applied and the influence of virtual resistance is studied. All these works have shown that the virtual resistance improves the VSM robustness during transient events. However, a virtual resistance would be probably insufficient to fulfill all the requirements imposed by grid codes. The virtual impedance is an important tool for VSMs. It is used to modify the dynamic response of grid-tied converters working either in grid-following or grid-forming mode. However, the functionality of the virtual impedance varies depending on the grid strength and the type of controller. In weak grids, the virtual impedance can be used to enhance the stability properties of grid-following converters [24]. In contrast, for grid-forming converters, the virtual impedance usually helps in the case of stiff grids [25]. Alternatively, some authors have proposed to adapt the virtual impedance according to the grid conditions [26].

C. Contributions

In this article, two control alternatives for implementing the VSM control technique in type-III wind turbines are proposed and analyzed. A traditional vector current controller is used in both alternatives so that the internal current control structure is not modified. Therefore, the type-III wind turbine can provide grid-forming capability while maintaining all the functionalities of conventional current controllers. In addition, a novel

flux-based virtual inductance is proposed and included in one of the control alternatives. Then, the operation of a wind farm formed by six DFIGs connected in parallel is analyzed for both control alternatives. In particular, the stability of the wind farm is studied for variations of the system parameters by using small-signal tools. Grid-connected and island operation modes are explored. Also, some design recommendations are provided for the virtual impedance in order to improve the system robustness. The operation of the wind farm is verified by using real-time simulations performed in OPAL-RT. Finally, the VSM controllers are verified in a laboratory setup with a real 28 kVA DFIG. The contents of this article have been applied in a PTC patent before its publication [27].

D. Organization

The rest of this article is organized as follows. In Section II, the application and the modeling strategy are described. In Section III, the control alternatives are presented. In Section IV, the two control alternatives are applied in the context of a wind farm. The wind farm operation is validated in Section IV-D by using real-time simulations. Experimental results are presented in Section V. Finally, Section VI concludes this article.

II. SYSTEM OVERVIEW

A. Application Description

Fig. 1 shows the electrical and control diagram of one wind turbine while Fig. 2 shows the electrical diagram of the system under study. It consists of a wind farm formed by six type-III wind turbines connected in parallel. The coupling transformer and the electrical line of each wind turbine are modeled with an RL circuit. The wind farm can work either connected or disconnected from the main grid, forming an electrical island. Each wind turbine consists of a DFIG. The stator is directly connected to the grid and the rotor is fed by a back-to-back (BTB) converter. The other side of the BTB converter is connected to grid via an L or an LC filter, depending on the control alternative.

Fig. 1 shows the control diagram of one wind turbine. The controller is divided in two parts: the RSC controller and the GSC controller. The RSC is controlled as a VSM so that the wind turbine is able to form grids. The VSM consists of an external active-power controller that generates the virtual-shaft angle (θ_s) and a reactive-power controller that generates the module of the virtual flux (ψ_v). The RSC also has internal controllers and their configuration depends on the control alternative. The description of the active and reactive power controllers, the parameters J_V, D_p, K_Q, and D_q, and the rest of signals involved is not included here for brevity (it can be found in [12]).

The GSC controller includes a standard vector current controller and a dc-link voltage controller. The current controller decouples the control of the active and the reactive power exchanged between the converter and the grid. The dc-link voltage controller calculates the active power required to maintain the dc-bus voltage (u_{dc}) constant while the reactive power command can be set freely (in this article, it will always be set to zero for simplicity). The current references ($\vec{i}_f^*$) are obtained by inverting
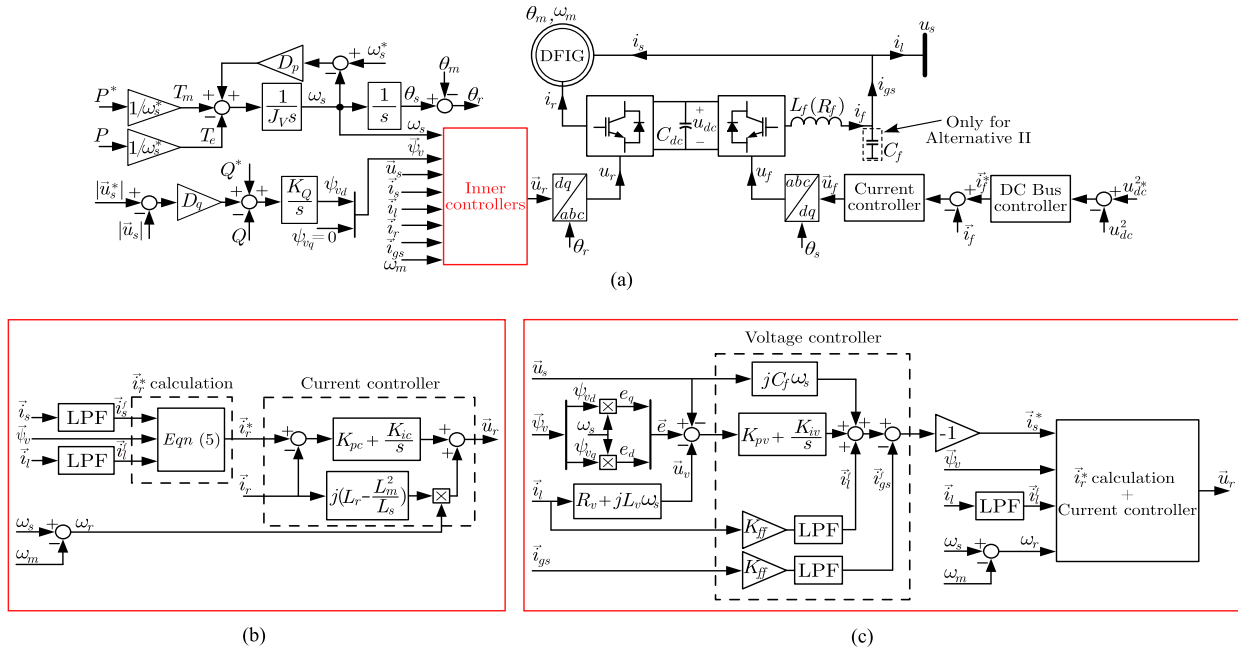
Fig. 1.   Electrical and control diagram of one wind generator. (a) General overview. Alternatives (b) I and (c) II for the control of the RSC.
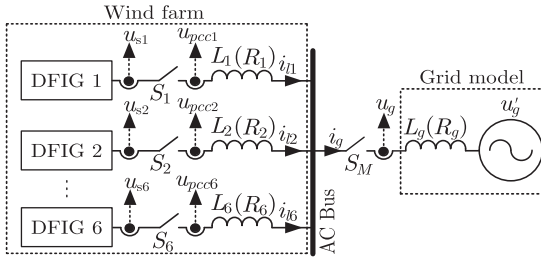

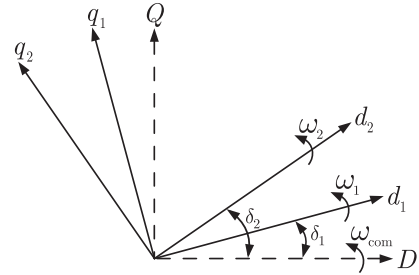Fig. 2.   Electrical diagram of the application studied in this work.

Fig. 3.   Rotating reference frames used to model the wind farm.

the power expressions, as it is common in the literature [28]. The angle of the VSM is used to perform the Park's transformations of the GSC controller as this makes the system more robust in weak grids. In the rest of this article, an arrow over a variable name indicates a space vector in a dq reference frame (e.g., $\vec{i}_f = i_{fd} + ji_{fq}$).

B. State-Space Modeling

Each DFIG is modeled on a synchronous reference frame (SRF) (dq_n), which is synchronized with the d-axis of the virtual flux generated by its own VSM $(\vec{\psi}_{vn})$ and, therefore, has the rotation speed of its virtual shaft. All the models are combined in a common reference frame (DQ) by using a rotation matrix. The SRF of the grid voltage is used as the reference in grid-connected mode [29]. In island mode, the SRF of the first DFIG is used as the reference [30]. Fig. 3 shows this concept, graphically. The angle used for the rotations is

$$\delta_n = \theta_n - \theta_{\text{com}} \tag{1}$$

where δ_n is the angular difference between the SRF of the nth DFIG (θ_n) and the common reference frame (θ_{com}).

III.   CONTROL ALTERNATIVES FOR THE RSC

A. Alternative I: Current Control With Novel Flux-Based Virtual Inductance

Fig. 1(b) shows the control diagram of this alternative. It includes a current controller and the set of equations for calculating the current reference. In these equations, the reference of the rotor current $(\vec{i}_r^*)$ is linked with the virtual flux of the VSM. This allows to replicate the effect of a virtual inductance by using the line current $(\vec{i}_l)$. The detailed procedure is explained in the following paragraph.

Fig. 4(a) shows an equivalent electrical circuit of the DFIG including the iron losses, where all the variables are referred to the stator [4]. According to this equivalent circuit, the stator flux can be calculated as follows:

$$\vec{\psi}_s = L_s\vec{i}_s + L_m(\vec{i}_r - \vec{i}_{\text{fe}}) \tag{2}$$

where L_m is the magnetizing inductance, L_s is the stator inductance $(L_s = L_{\sigma s} + L_m)$, and $L_{\sigma s}$ is the leakage inductance. The variable $\vec{i}_{\text{fe}}$ models the iron losses and it can be calculated
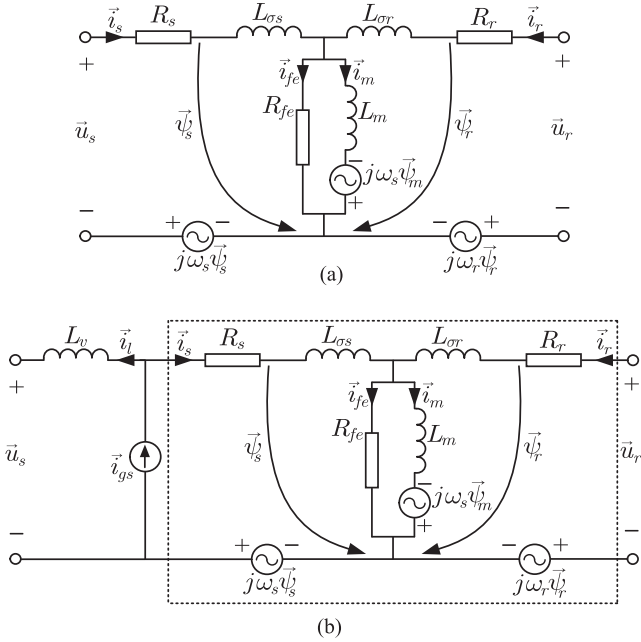
Fig. 4.   Model of a DFIG in a dq reference frame (a) without and (b) with the flux-based virtual inductance.

as follows [31]:

$$\vec{i}_{\text{fe}} \approx j\frac{\omega_s}{R_{\text{fe}}}(\vec{\psi}_s - L_{\sigma s}\vec{i}_s) \tag{3}$$

where R_{fe} is the equivalent "iron resistance." Iron losses are commonly neglected in high-power DFIGs. However, losses might be significant in low-power machines. Therefore, if (2) is used to estimate the stator flux, the literature recommends considering them [4].

The virtual inductance will be implemented by adding a term to the stator flux in (2), resulting the "virtual stator flux":

$$\vec{\psi}_{sv} = L_s\vec{i}_s + L_m(\vec{i}_r - \vec{i}_{\text{fe}}) + L_v\vec{i}_l. \tag{4}$$

Fig. 4(b) shows the modified equivalent circuit of the induction generator when the virtual inductance is included. There is a current source $(\vec{i}_{gs})$, which accounts for the effect of the grid-side converter current. The aim of the grid-side converter is to maintain the dc voltage constant. Therefore, the effect over the machine dynamics is commonly neglected and it can be considered that L_v is in series with $L_{\sigma s}$. It can be seen that increasing L_v has the same effect as increasing L_s. For the implementation, as the current controller regulates $\vec{i}_r$, the reference for that current should be calculated by using (4), yielding

$$\vec{i}_r^* = \frac{\vec{\psi}_{sv} - L_v\vec{i}_l - L_s\vec{i}_s + L_m\vec{i}_{\text{fe}}}{L_m}. \tag{5}$$

For calculating (5), the value of the stator virtual flux is required. To simplify the developments, it was made equal and aligned with the virtual flux of the VSM. Therefore,

$$\vec{\psi}_{sv} = \psi_v. \tag{6}$$

The proposed flux-based virtual inductance is a novel contribution of this work and it is part of a PTC patent [27].

B. Alternative II: Voltage Controller, Current Controller, and Virtual Impedance

Fig. 1(c) shows the block diagram of this control alternative. A voltage controller is added on top of the current controller to regulate the stator voltage. A capacitor was added to the GSC filter so that the voltage is easier to control [28]. The voltage controller consists of a PI controller plus the feedforward terms applied to $\vec{i}_l$ and $\vec{i}_{gs}$. A low-pass filter and a gain $(0 < K_{ff} < 1)$ was used in the feedforwards to avoid high-frequency interactions. The "minus" in the output of the voltage controller is used to be consistent with the sign criterion of the rest of the control system. The reference for the voltage controller is calculated by multiplying ψ_v and ω_s [12]. The structure of the current controller and the reference of the rotor current are kept as in Alternative I. However, in this case, the stator current $(\vec{i}_s)$ is replaced by the reference calculated by the voltage controller $(\vec{i}_s^*)$. Therefore, a low-pass filter is not needed.

The virtual impedance is a useful tool since it simplifies the parallel interconnection of power converters. Here, it is implemented by adding a term $(\vec{u}_v)$ to the original reference generated by the VSM $(\vec{e})$ [32]. Virtual resistance can also be added.

C. Precision of the Current Reference Calculation

The values of L_s and L_m and the iron losses are required to calculate the current reference (i_r^*). Commonly, these values are obtained in a series of preliminary tests performed before the commissioning of the wind turbine. If these values are not correctly estimated, the control performance would be affected in different ways. First, there would be inaccuracies in the estimated flux, which are translated as errors in the orientation of the reference frame. Therefore, the accuracy of the torque control would be reduced [4]. It is worth noting that these errors do not commonly result in instabilities, but they degrade the overall control performance.

The impact of these inaccuracies is different depending on the control alternative. For Alternative I, which is based on a flux-oriented vector control, the inaccuracies in the torque control are directly reflected in the transient response. Conversely, for Alternative II, the orientation of the vector control relies on the estimated voltage. This implies that the voltage controller helps in maintaining the dq reference frame alignment. Consequently, the inaccuracies of the torque controller are effectively compensated, thereby alleviating their negative impact in the control performance.

IV. ANALYSIS OF A WIND FARM WITH THE TWO CONTROL ALTERNATIVES

In this section, the performance of both control alternatives is analyzed against variations in the system parameters. The system consists of six DFIGs that operate in parallel configuration and can work either connected or disconnected from the grid. For

TABLE I
ELECTRICAL PARAMETERS OF THE TEST SYSTEM

Var.	Value	Var.	Value	Var.	Value
X_g	0.1 pu	R_g	pu	C_f	100 μF
X_l	0.02 pu	R_l	pu	C_{dc}	2.25 mF
L_f	0.75 mH	R_f	0.024 Ω	L_m	0.04 H
$L_{\sigma s}$	1.63 mH	$L_{\sigma r}$	1.63 mH	R_s	0.097 Ω
R_r	0.18 Ω	R_{fe}	84.3 Ω	V_{dc}	700 V
f_n	50 Hz	V_n	400 V	S_n	28.7 kVA

TABLE II
CONTROL PARAMETERS OF THE TEST SYSTEM

Var.	Value	Var.	Value	Var.	Value
L_v^{AI}	2 mH	R_v^{AI}	0 Ω	L_v^{AII}	4 mH
R_v^{AII}	0.31 Ω	J_V	65	D_P	300
K_Q	8.75 $\cdot 10^{-6}$	D_Q	400	ω_{Bgcc}	225 Hz
ω_{Brcc}	225 Hz	ω_{Brvc}	22 Hz	ω_{Bdc}	11 Hz

the sake of simplicity, all the wind turbines have the same parameters. For both alternatives, the controllers are designed with the goal of achieving a robust design. Subsequently, the stability properties of the alternatives is analyzed by using small-signal analysis and admittance analysis. Finally, the results are validated through real-time simulations.

A. Design of Controllers

In order to achieve a robust design for both control alternatives, the following design steps were followed. Initially, the controllers of the GSC were designed. The GSC controllers are identical for both alternatives. Subsequently, the rotor current controller was designed following traditional methods, as described in [4]. This controller is also the same for both alternatives. Then, the voltage controller for Alternative II was designed. The bandwidth of this controller was selected ten times less compared with the current controller. This criterion ensures sufficient bandwidth separation between the current and the voltage controller, and it is a common approach for designing cascaded controllers. Then, the parameters of VSM were chosen to meet specified settling times and damping factors [33]. Finally, the virtual impedance was selected according to the results presented in Section IV-B3.

B. Small-Signal Analysis

1) Small-Signal Model Development: A detailed small-signal model of the wind farm was developed for conducting this analysis. This model was developed in continuous time. The model includes the RSC and the GSC controllers, plus implementation details, such as time delays and an equivalent function that models the pulsewidth modulation [34]. All hardware elements are also included. A sixth-order model was used for the electrical machine (the iron losses were considered). The procedure for deriving the small-signal model is based on the method presented in [30]. The main hardware parameters are given in Table I, while the control parameters are given in Table II.

The most representative eigenvalues were extracted by using participation factors and are listed in Table III. The base designs for Alternatives I and II were used to calculate these eigenvalues.

TABLE III
MODES AND MOST RELEVANT STATES AFFECTING THEM

Eig.	Grid-connected mode			Island mode		
λ	ω_n	ζ	States	ω_n	ζ	States
1,2	432	0.35	$\vec{i}_g$	261	0.61	$\vec{i}_f, x_{gccd}, x_{dld}$
3,4	330	0.28	$\vec{i}_g$	190	0.62	x_{gccq}
5,6	51.2	0.02	i_m, i_{gq}	57.61	0.19	i_{md}, x_{rccd}
7,8	51	0.01	$\vec{i}_m$	50.93	0.01	$\vec{i}_m$
9,10	42.81	0.69	i_{sq}^f	31.04	0.76	i_{sq}^f
11,12	9.13	0.35	$\vec{x}_{rvc}$	11.55	0.42	$\vec{x}_{rvc}$
13,14	8.46	0.35	$\vec{x}_{rvc}$	8.4	0.34	$\vec{x}_{rvc}$
15,16	0.49	0.69	θ_s, ω_s	0.47	0.67	θ_s, ω_s
17	0.41	1	$\vec{\psi}_v, \omega_s$	0.33	1	$\vec{\psi}_v$
18,19*	0.36	0.89	θ_s, ω_s	0.73	1	ω_s
20	0.36	1	$\vec{\psi}_v$	0.38	1	$\vec{\psi}_v, \theta_s$

*In island mode, λ19 does not exist.

Only the states with participation factors above 0.8 are shown. Among them, $\vec{x}_{dl}$ is the state related to the computational delay of the grid-side converter, $\vec{x}_{rvc}$ is the state related to integral of the voltage controller, and $\vec{x}_{rcc}$ and $\vec{x}_{gcc}$ are the states related to the integrals of the RSC and the GSC controllers. The rest of symbols were presented in previous sections.

2) Weak Grid Effect: The results presented here highlight the differences between the alternatives in the case of weak grids. Fig. 5 shows the system eigenvalues when the grid SCR varies between (red) 10 and (green) 1. In Fig. 5(a)–(c), results for Alternative I are shown, while those for Alternative II are shown in Fig. 5(d)–5(f). In Fig. 5(a) and (d), there are two pairs of complex eigenvalues in the high-frequency range whose frequency decreases as the grid impedance increases. This high-frequency resonance is common in system with long transmission cables [35]. In both cases, relevant stability issues were not found.

Fig. 5(b) shows the medium-frequency eigenvalues for Alternative I, where two pairs of poorly damped complex eigenvalues can be observed in the surroundings of 50 Hz. The pair that varies its position is related to the interaction between the DFIGs and the grid voltage, while the one that remains constant is related to the interaction between the DFIGs. Clearly, DFIGs are sensitive to grid disturbances (this was already noticed in [4]).

Fig. 5(e) shows the medium-frequency eigenvalues for Alternative II. Here, two additional pairs can be observed. These appear due to the interaction between the voltage controllers and the grid [12], [36]. As the grid becomes weaker, these eigenvalues become better damped. Therefore, the alternative based on the voltage controller is prone to subsynchronous resonances in stiff grids, and for that case, a robust design of the voltage controller and the virtual impedance is required [12].

Fig. 5(c) and (f) shows the eigenvalues related to the VSMs dynamics. These dynamics are very similar for both alternatives. The low-frequency oscillatory (complex) modes represent the link between the VSMs and the grid and are related to the power-frequency dynamics. They become slower and more damped as the grid impedance increases. Meanwhile, the real modes (related to the voltage dynamics) become faster. Oscillatory modes between VSMs remain almost constant.

3) Virtual Inductance (L_v) Effect: Fig. 6(a) shows the system medium-frequency eigenvalues when the virtual inductance
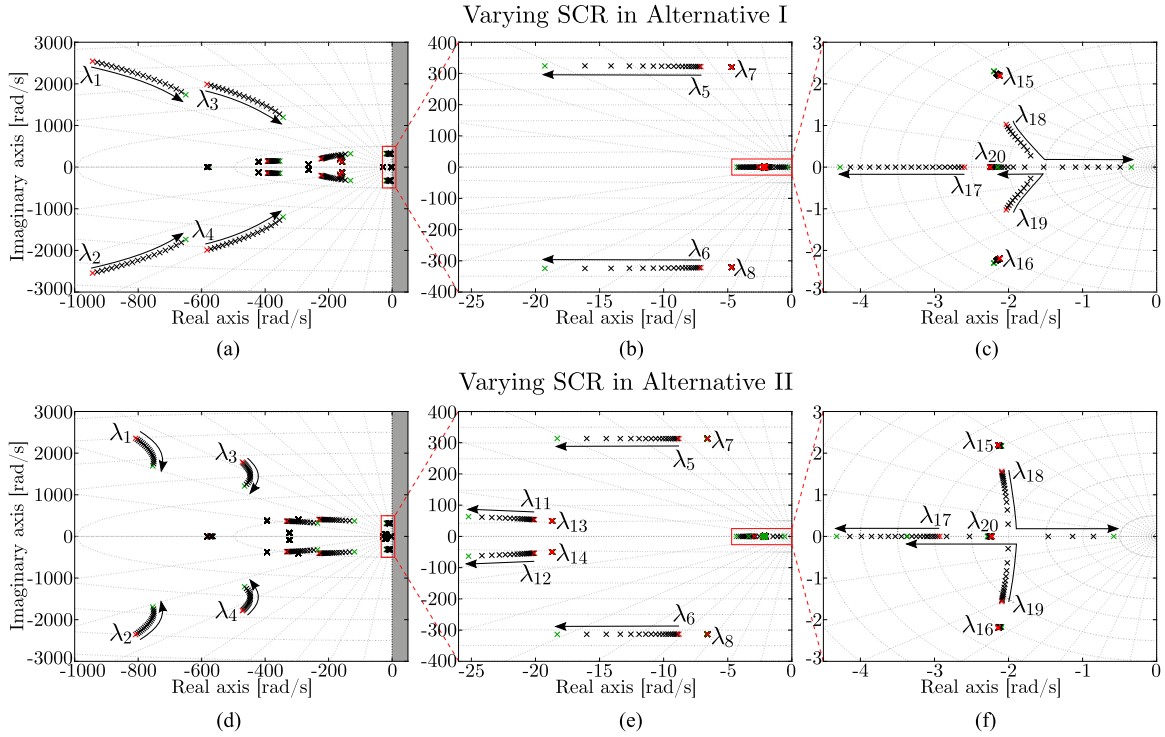
Fig. 5. Eigenvalues of the wind farm for grid-connected mode when the SCR varies between (red) 10 and (green) 1. Alternatives (a)–(c) I and (d)–(f) II.
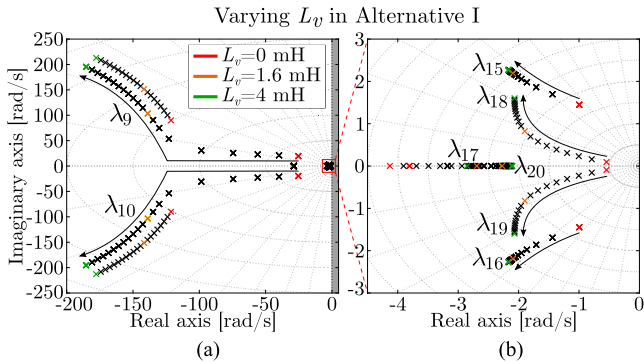

Fig. 6. Low-frequency eigenvalues of the wind farm when L_v varies between (red) 0 and (green) 4 mH for Alternative I.
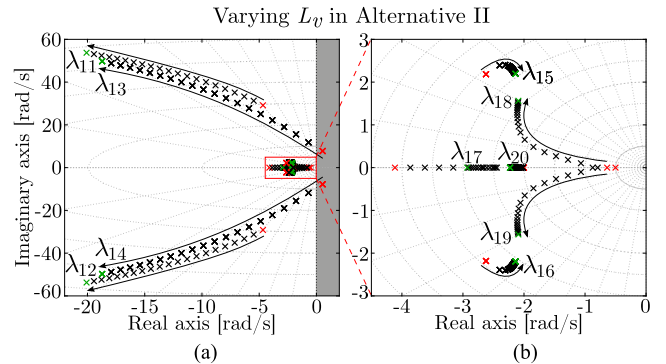
Fig. 7. Low-frequency eigenvalues of the wind farm when L_v varies between (red) 0 and (green) 4 mH for Alternative II. $X/R = 4$ for L_v.

value varies between (red) 0 and (green) 4 mH, for Alternative I. There is a pair of complex eigenvalues moving away from the imaginary axis as L_v increases. These eigenvalues are related to the stator currents, which are the "output" variables of DFIGs and, therefore, the source of interactions. As the lines between the DFIGs are short (see Table I), the virtual impedance greatly helps in avoiding interactions since it virtually increases the electrical distance between them. In this regard, Fig. 6(b) shows the low-frequency eigenvalues for Alternative I. As the VSMs parameters were designed without taking into consideration any other element in the system, the low-frequency interactions between DFIGs modify the location of these eigenvalues. This effect is undesirable and should be avoided. For $L_v > 1.6$ mH, the coupling is avoided and these eigenvalues do not significantly change their location. In the case of the oscillatory modes

between the VSMs and the grid, they become less damped and faster as L_v increases, while the real modes become slower.

Fig. 7(a) shows the system medium-frequency eigenvalues for Alternative II. In this case, small values of L_v lead to a poor damping of the subsynchronous resonance related to the voltage controllers that might even lead to instability. The resonance frequency is close to the VSM bandwidth for these values, causing low-frequency interactions with the VSM dynamics. This modifies the location of the VSM eigenvalues, as shown in Fig. 7(b). The oscillatory modes between the VSMs and the grid are similar to those of Alternative I.

Based on these results, the following recommendations are made for choosing L_v.

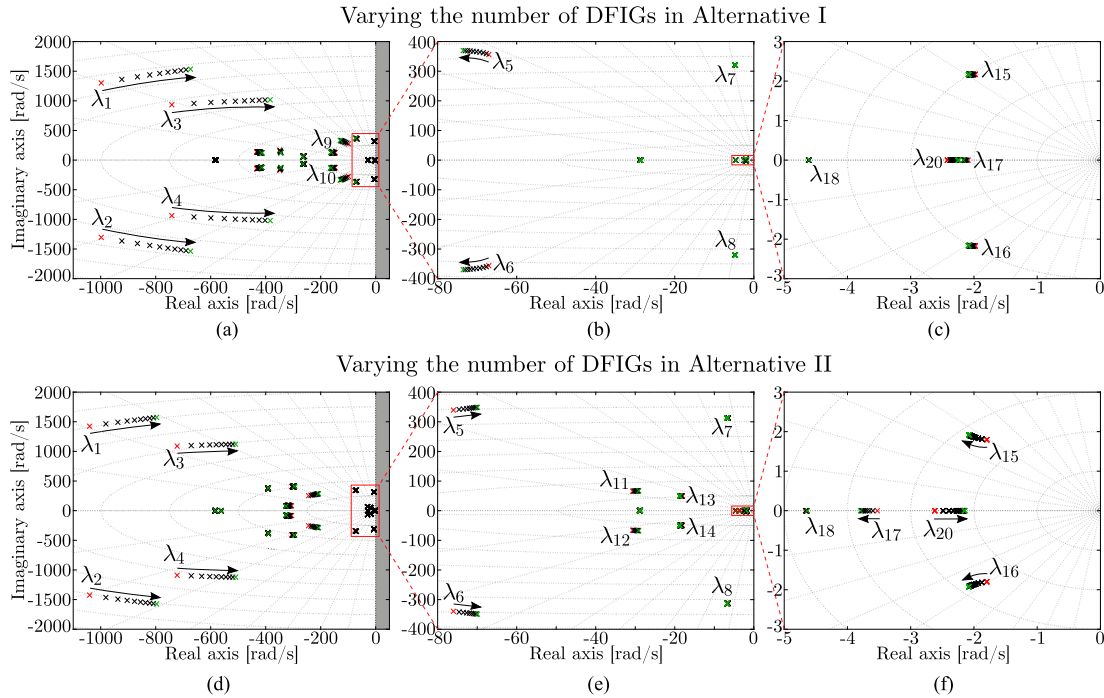1) For Alternative I, L_v should be large enough to avoid slow-frequency interactions between VSMs.

Fig. 8. System eigenvalues in island mode. The number of DFIGs varies between (red) 6 and (green) 15. Alternatives (a)–(c) I and (d)–(f) II.

2) For Alternative II, L_v should be large enough to ensure that the subsynchronous resonance is well damped. A damping factor (ξ) higher than 0.25 is recommended.

3) In both cases, the value of L_v should be as low as possible to avoid the practical drawbacks of large virtual impedances.

It is worth mentioning that the bandwidth of the voltage controller also plays a key role in the damping of the subsynchronous resonance. Insufficient time-constant separation between the VSM and the voltage controller significantly affects it (the larger the bandwidth of the voltage controllers, the more damped the resonance will be [12]).

4) Effect of the Number of DFIGs in Island Mode: Fig. 8 shows the system eigenvalues in island mode when the number of DFIGs varies between (red) 6 and (green) 15. In the high-frequency range, both alternatives exhibit similar performance. There are two pairs of complex eigenvalues that move toward instability as the number of DFIGs increases. Although Alternative I is slightly more sensitive to the number of DFIGs in this frequency range, the system stability margins are not significantly affected.

Fig. 8(b) and (e) shows the medium-frequency eigenvalues for Alternatives I and II, respectively. There is a pair of complex eigenvalues that moves away from the imaginary axis for Alternative I, and the behavior is the opposite for Alternative II. These eigenvalues are related to the interaction between the DFIGs and the PCC voltage. Unlike in grid-connected operation [see Fig. 5(b) and (e)], this resonance is well damped due to the resistive nature of the load. For the rest of medium-frequency dynamics, significant differences were not observed. The eigenvalues related to the VSMs dynamics [see Fig. 8(c) and (f)] are maintained constant for Alternative I, while they slightly vary for

Alternative II. Also, a relevant change can be seen with respect to grid-connected operation, for both Alternatives I and II. Instead of a pair of oscillatory modes, only one real mode appears as a result of the power–frequency interaction between the VSMs and the PCC (as the grid is no longer there, the VSMs do not oscillate against it).

C. Admittance Analysis of the Wind Farm

The models obtained in Section IV-B1 were adapted here to analyze the admittance of the control alternatives. This means that the level of detail is similar to that of the state-space model described in the previous section. The system and control parameters were also the same, and are listed in Tables I and II. The input admittance of the wind farm is first derived as a real space-vector model in a dq reference frame

$$\begin{bmatrix} i_g^d \\ i_g^q \end{bmatrix} = \begin{bmatrix} G_{dd}(s) & G_{dq}(s) \\ G_{qd}(s) & G_{qq}(s) \end{bmatrix} \begin{bmatrix} u_g^d \\ u_g^q \end{bmatrix}. \quad (7)$$

As the DFIG equations of the d- and q-axes are different (mainly due to the VSM), the admittance is asymmetric. Therefore, the method described in [37] for modeling complex asymmetric vector systems was used. This method allows the use of single input single output (SISO) techniques for stability analysis at the expense of using an asymmetric complex SISO model [38]. Here, only the symmetric part has been analyzed since the antisymmetric part was less relevant. There are other methods available to calculate and analyze the impedance of electronic devices. In particular, the system equations are often modeled in the dq domain [39]. This impedance in the dq domain can be translated to sequence domain by using matrix transformations. The differences between these methods can be found in [40].
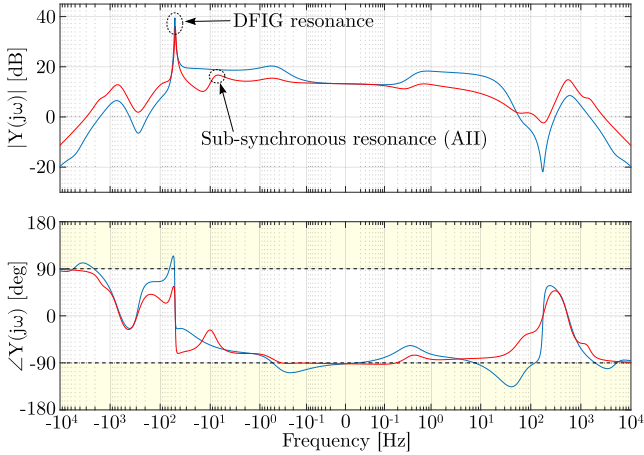
Fig. 9. Bode plots of the wind farm admittance. Alternatives (blue) I and (red) II.

Fig. 9 shows the Bode plots of the wind farm input admittance for Alternatives (blue) I and (red) II. The resonance caused by the magnetizing inductance appears at -51 Hz. Also, the subsynchronous resonance caused by the voltage controller in Alternative II appears at around -7 Hz. As L_v was chosen to avoid problems at this frequency, the resonance is well damped. Alternative II is passive in the whole frequency range (i.e., $-90° < \angle Y(j\omega) < 90°$), except in the very low-frequency range (this cannot be avoided since it depends on the VSM). Passivity is important for interconnected systems since it avoids instabilities [41].

It is important to note that passivity is highly dependent on the controller architecture, the numerical values of the control parameters and the hardware elements. Therefore, it is not straightforward to judge which control alternative has better passivity properties.

D. Validation in Real-Time Simulations

The effectiveness of Alternatives I and II was tested in OPAL-RT for six DFIG operating in parallel. The impact of the virtual impedance value was carefully evaluated.

1) Parallel Operation With Alternative I: Fig. 10 shows the active and reactive powers injected by the DFIG when a 10 kW step change was applied in P^*, for different values of L_v. For values of L_v of 1.6 and 4 mH, the transient responses are similar. However, when $L_v = 0$ mH, the transient becomes slower. Also, active and reactive powers present more coupling in the latter case. The virtual flux is slightly different in the steady state. This happens because the virtual impedance value modifies the voltage command of the VSM. These results are in accordance with the theoretical analysis presented in Section IV-B3.

2) L_v Effect in Alternative II: Fig. 11 shows the active and reactive powers of the DFIGs when the voltage level is reduced to 85% of its nominal value, for different values of L_v. The purpose of applying this small voltage variation is to show the subsynchronous resonance. The six DFIGs were operating in parallel and connected to the grid. For $L_v = 4$ mH (robust design), only the 50 Hz resonance can be observed in both
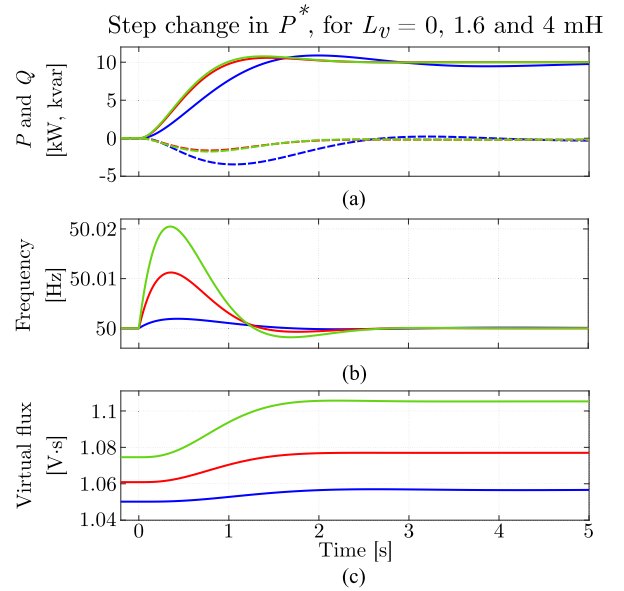

Fig. 10. Results of the wind farm obtained with OPAL-RT. Transient responses of one DFIG for a step change in P^*, for different values of L_v. L_v is set to (blue), (red) 1.6, and (green) 4 mH. (a) (Solid) Active and (dashed) reactive power.
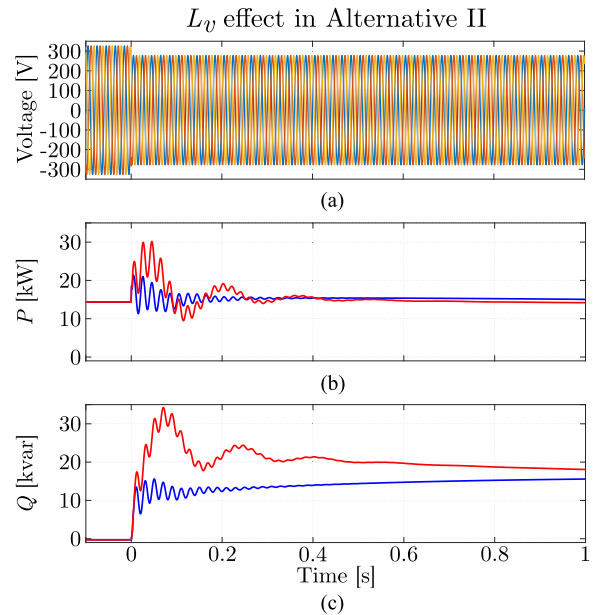

Fig. 11. Results obtained with OPAL-RT. Transient responses of one DFIG for a variation of the grid voltage, when L_v is set to (red) 1 and (blue) 4 mH.

active and reactive power transients. However, for $L_v = 1$ mH the subsynchronous resonance is not well damped. This causes a transient power injection that produces overcurrents in the rotor windings. These results are in accordance with the theoretical analysis presented in Section IV-B3.

3) Sudden Disconnection From the Main Grid: Fig. 12 shows the transient responses of (a) the voltage module and (b) the frequency of the PCC, for Alternatives (blue) I and (red) II, when the connection to the grid was suddenly lost. At that moment, each wind turbine was operating at 50% of
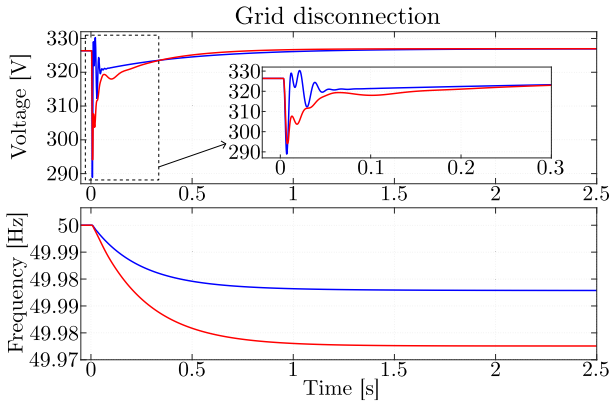
Fig. 12. Transient responses of the wind park when it is suddenly disconnected from the main grid. Alternatives (blue) I and (red) II.
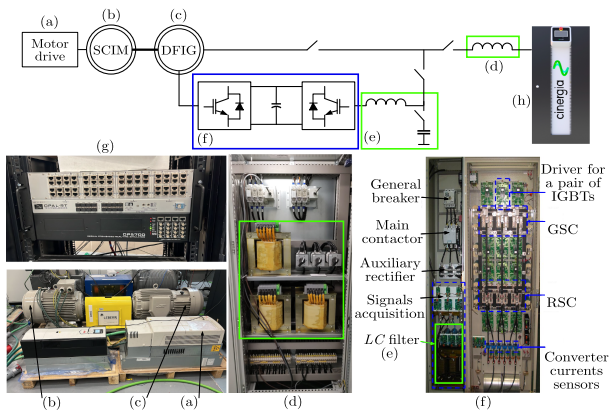

Fig. 13. Laboratory facilities. (Top) Electrical diagram of the laboratory and (bottom) photographs. (a) Motor drive. (b) SCIM. (c) DFIG. (d) Grid impedance. (e) GSC filter. (f) VSCs. (g) Hardware-in-the-loop platform (OPAL-RT). (h) Three-phase voltage source.
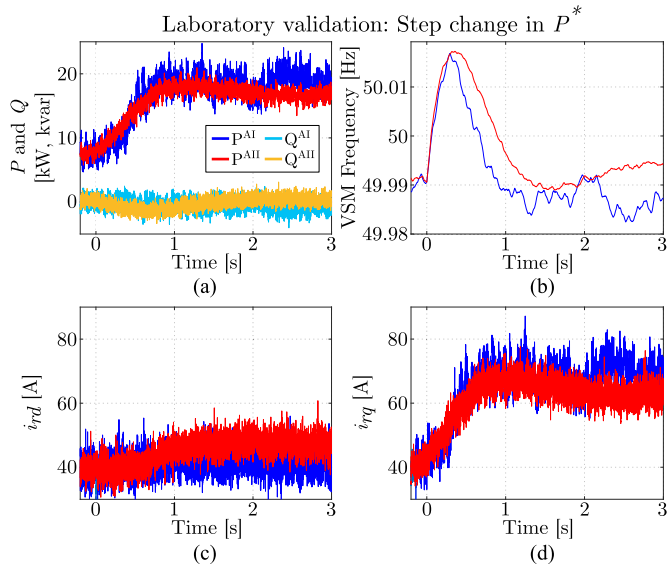

Fig. 14. Experimental validation of Alternatives I and II. Transient responses for step changes in P^*. (a) P and Q for Alternatives (blue, cyan) I and (red, yellow) II. (b) VSM frequency. (c) d-axis. (d) q-axis rotor current. Alternatives (blue) I and (red) II.
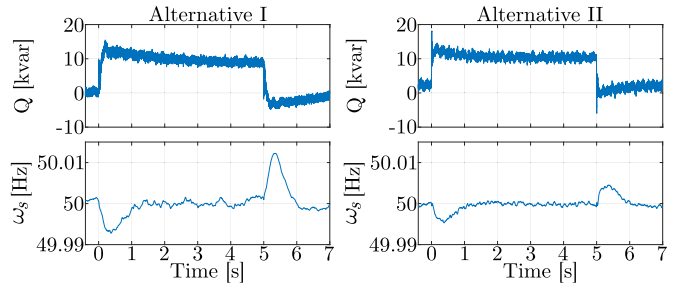

Fig. 15. Experimental validation of Alternatives I and II. Transient responses for a 10% reduction of the grid voltage, for 5 s. Alternatives (left) I and (right) II.
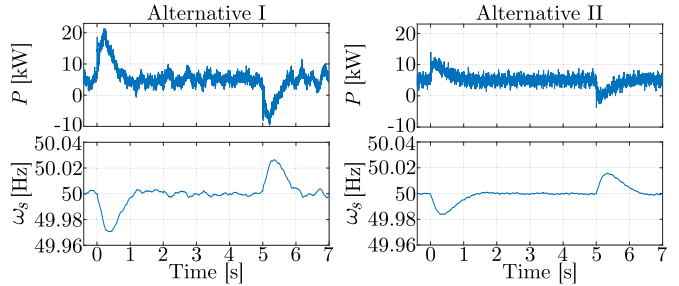

Fig. 16. Experimental validation of Alternatives I and II. Transient responses for a negative phase jump of five degrees in the grid voltage. Another phase jump of five degrees is applied in the opposite direction, after 5 s. Alternatives (left) I and (right) II.

its rated capacity, while the load rating was 100% of the wind farm capacity. This means that each DFIG suddenly changed its power injection from 50% to 100% of its rated capacity. The source of the power injected is not discussed here since the main objective is to analyze the dynamic characteristics of the grid-forming alternatives. The PCC voltage module drops to 89% for Alternative I, and to 90 % for Alternative II. Both alternatives are able to quickly restore the voltage, although Alternative I is slightly faster. Besides, the transient responses of the frequency exhibit an adequate performance. The frequency drops slightly more for Alternative II because in this case the virtual impedance is larger. Also, it can be observed that the frequency does not return to its original value. This is expected as the system is operating as an electrical island and the VSMs have droop terms. It should be noted that in a real application, a secondary controller is commonly added to restore the frequency (e.g., a power plant controller).

V. EXPERIMENTAL VALIDATION

A. Experimental Platform

The proposed control alternatives were tested in the GEISER research group facilities at Alcalá de Henares University. Fig. 13 shows an electrical diagram of the laboratory, together with some photographs of the main elements. The experimental prototype consists of a 150 kVA three-phase back-to-back neutral-point clamped (NPC) VSC and a DFIG driven by a 28.7 kVA squirrel cage induction machine, which emulates the wind turbine. The main hardware parameters are shown in Table I. The
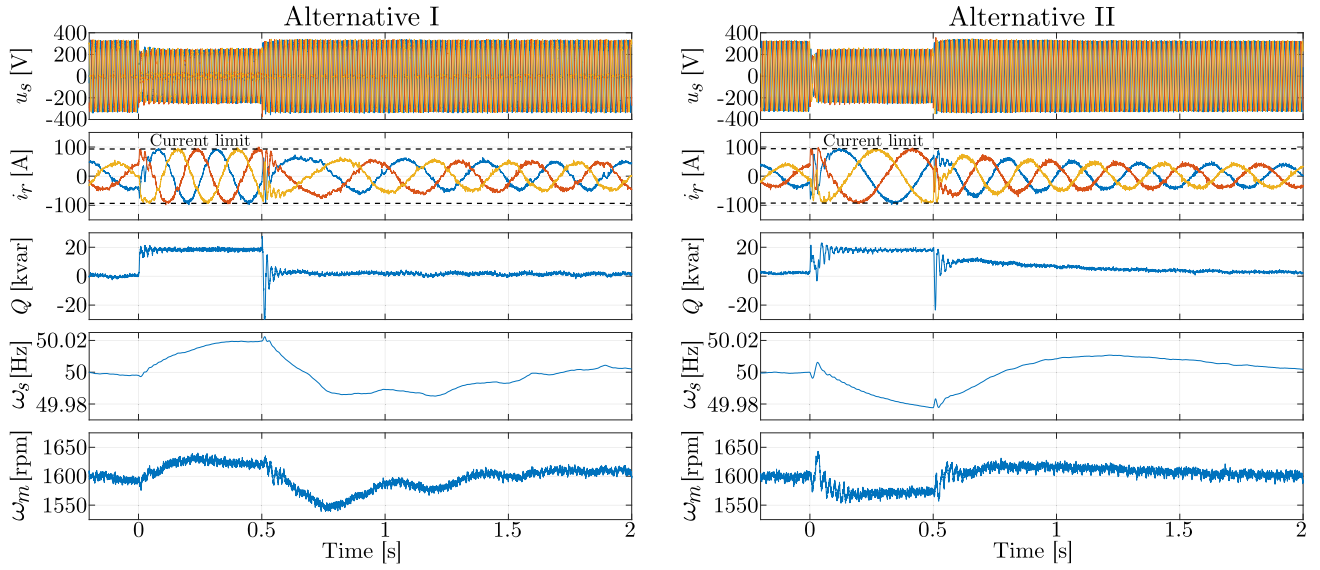
Fig. 17. Experimental validation of Alternatives I and II. Transient responses for a 65% voltage dip. Alternatives (left) I and (right) II.

control system was implemented in a digital signal processor (TMS320C6713) from Texas Instruments and a FPGA (SPARTAN 3E) from Xilinx. The sampling and switching frequencies were 10 kHz and 5 kHz, respectively. The control parameters are shown in Table II. See [42] for more details of the hardware and software platforms.

B. Experimental Results

1) Step Changes in P^*: Fig. 14 shows the transient response of the DFIG when it was connected to the grid and a 10 kW step change was applied to P^*. For this particular test, the values of the virtual impedances for the two alternatives were made equal. As a consequence, the responses to the power steps should have a similar shape and the time responses can be easily compared. For the rest of the tests presented in this section, the virtual impedances obtained during the design procedure were used. It can be seen that both alternatives provide similar results. The initial value of the VSM frequency was 49.99 Hz. In the peak of the response, a value of 50.016 Hz is reached in both cases. However, in Alternative I, the effect of noise is more relevant. This happens because the DFIG used in the laboratory is not well aligned and this causes oscillations in the stator currents. As Alternative I uses the stator currents for calculating the rotor current references, this effect is amplified. It should be noted that this effect would not happen in a DFIG with more inertia (i.e., in a wind turbine) and a well-aligned shaft.

2) Response to a Variation of the Grid Voltage: Fig. 15 shows the transient response of the DFIG when the grid voltage is reduced, for 5 s. It can be seen that the DFIG quickly reacts to that disturbance by increasing the reactive power injection in 10 kvar. This value is similar for the two alternatives. Such behavior demonstrates the capability of the DFIG to provide grid voltage support. When the voltage level is restored, the reactive power goes back to its previous value. Small transients can also be observed in the VSM frequency (the peaks in Alternative I are

40% larger compared with Alternative II). This happens because the active power slightly varies during grid voltage transients. Also, it can be seen that these transients were less pronounced in Alternative II. This happens because the virtual impedance is larger for this alternative and, as a consequence, the variation in the frequency is smaller.

3) Response to a Phase Jump: Fig. 16 shows the transient responses of the DFIG when a negative phase jump of five degrees was applied in the grid voltage. Another phase jump of five degrees was applied in the opposite direction, after 5 s. It can be seen that the active power increases in response to the negative phase jump and it decreases in response to the positive phase jump. In addition, it can be noticed that the active power reaches higher values in the case of Alternative I (20 and 12 kW for Alternative I). This happens because in Alternative II the virtual impedance value is larger compared to that of Alternative I. As a consequence, the frequency variation for Alternative I is larger. These results highlight the role of the virtual impedance when DFIGs are operating in grid forming mode.

4) Rotor Current Saturation: Fig. 17 shows the transient response of the DFIG when a 65% three-phase voltage dip is applied to the grid voltage. For this dip depth and level of power, the rotor current saturates. Consequently, the capability of the DFIG to support the stator voltage is curtailed, as the generation of reactive power is inherently linked to the rotor current. The limitation of the rotor current acts as a protection and safeguards the integrity of power converters. This is possible because both alternatives have a current controller in the RSC. Also, it can be observed that there is a 50 Hz oscillation that appears after the beginning of the transient, for both alternatives. This resonance was analyzed in Section IV-C. It can be easily noticed that the VSM frequency and the machine speed of the two alternatives are different during the voltage dip (the frequency changes in opposite directions). This difference is related to the way the controller saturates. In particular, for Alternative I, this saturation is applied directly after the VSM. However, in Alternative

II, the saturation comes after the output of the voltage controller. These differences in the machine speed during the voltage dip are directly reflected in the frequency of the rotor currents. After the voltage dip, both the VSM frequency and the machine speed are restored to their previous value. Based on these results, the development of saturation strategies for the two alternatives is of interest for further research.

VI. Conclusion

In this article, two control alternatives for implementing a VSM controller without modifying the internal current controllers of type-III wind turbines have been proposed. These alternatives were tested in a wind farm consisting of six DFIGs. Eigenvalue and impedance analyses were performed. The operation of the wind farm was verified by using real-time simulations performed in OPAL-RT. Finally, the control alternatives were tested in laboratory, in a 28 kVA DFIG.

For the operation as a wind farm, the two control alternatives present differences in their eigenvalues loci. Both alternatives guarantee adequate stability margins in island mode. However, it is worth mentioning that Alternative I (which does not include a voltage controller) leads to very robust results in this case. It was shown that an adequate design of the virtual impedance is essential for Alternative I as it guarantees that the dynamics of DFIGs are decoupled. For the case of Alternative II, the virtual impedance was needed to avoid subsynchronous oscillations. From the impedance point of view, both alternatives led to robust designs. The results obtained from the real-time simulations verified the operation as a wind farm. The experimental results obtained in the hardware platform show that both control alternatives provided adequate results. Alternative I had more electromagnetic noise, although the low-frequency dynamics were similar in both cases. However, the control structure of Alternative I is simpler and therefore easier to implement. The developments and results presented in this article highlight the importance of the virtual impedance for type-III wind turbines controlled as VSMs. Also, the results presented in this work emphasize the usefulness of the current controller of the RSC.

References

[1] Y. Wu, S. Chang, and P. Mandal, "Grid-connected wind power plants: A survey on the integration requirements in modern grid codes," *IEEE Trans. Ind. Appl.*, vol. 55, no. 6, pp. 5584–5593, Nov./Dec. 2019.

[2] B. Pawar, E. I. Batzelis, S. Chakrabarti, and B. C. Pal, "Grid-forming control for solar PV systems with power reserves," *IEEE Trans. Sustain. Energy*, vol. 12, no. 4, pp. 1947–1959, Oct. 2021.

[3] A. Roscoe et al., "Response of a grid forming wind farm to system events, and the impact of external and internal damping," *IET Renewable Power Gener.*, vol. 14, no. 19, pp. 3908–3917, 2020.

[4] G. Abad, J. Lopez, M. Rodriguez, L. Marroyo, and G. Iwanski, *Doubly Fed Induction Machine: Modeling and Control for Wind Energy Generation*. Hoboken, NJ, USA: Wiley, 2011.

[5] S. Wang, J. Hu, and X. Yuan, "Virtual synchronous control for grid-connected DFIG-based wind turbines," *IEEE J. Emerg. Sel. Topics Power Electron.*, vol. 3, no. 4, pp. 932–944, Dec. 2015.

[6] K. D. Brabandere, "Voltage and frequency droop control in low voltage grids by distributed generators with inverter front-end," Ph.D. dissertation, KU Leuven, Leuven, Belgium, 2006.

[7] R. H. Lasseter, Z. Chen, and D. Pattabiraman, "Grid-forming inverters: A critical asset for the power grid," *IEEE J. Emerg. Sel. Topics Power Electron.*, vol. 8, no. 2, pp. 925–935, Jun. 2020.

[8] Q. Zhong and G. Weiss, "Synchronverters: Inverters that mimic synchronous generators," *IEEE Trans. Ind. Electron.*, vol. 58, no. 4, pp. 1259–1267, Apr. 2011.

[9] M. Chen, D. Zhou, and F. Blaabjerg, "Modelling, implementation, and assessment of virtual synchronous generator in power systems," *J. Modern Power Syst. Clean Energy*, vol. 8, no. 3, pp. 399–411, 2020.

[10] S. Dong and Y. C. Chen, "A method to directly compute synchronverter parameters for desired dynamic response," *IEEE Trans. Energy Convers.*, vol. 33, no. 2, pp. 814–825, Jun. 2018.

[11] J. Alipoor, Y. Miura, and T. Ise, "Power system stabilization using virtual synchronous generator with alternating moment of inertia," *IEEE J. Emerg. Sel. Topics Power Electron.*, vol. 3, no. 2, pp. 451–458, Jun. 2015.

[12] A. Gonzalez-Cajigas, J. Roldan Perez, and E. Bueno, "Design and analysis of parallel-connected grid-forming virtual synchronous machines for island and grid-connected applications," *IEEE Trans. Power Electron.*, vol. 37, no. 5, pp. 5107–5121, May 2022.

[13] S. Dong and Y. C. Chen, "Adjusting synchronverter dynamic response speed via damping correction loop," *IEEE Trans. Energy Convers.*, vol. 32, no. 2, pp. 608–619, Jun. 2017.

[14] S. D'Arco, J. Suul, and O. Fosso, "Small-signal modeling and parametric sensitivity of a virtual synchronous machine in islanded operation," *Int. J. Elect. Power Energy Syst.*, vol. 72, pp. 3–15, Nov. 2015.

[15] H. Wu et al., "Small-signal modeling and parameters design for virtual synchronous generators," *IEEE Trans. Ind. Electron.*, vol. 63, no. 7, pp. 4292–4303, Jul. 2016.

[16] H. Shao et al., "Equivalent modeling and comprehensive evaluation of inertia emulation control strategy for DFIG wind turbine generator," *IEEE Access*, vol. 7, pp. 64798–64811, 2019.

[17] National Grid ESO, "European connection conditions," 2018. [Online]. Available: https://www.nationalgrideso.com/document/107196/download

[18] J. Lopez, P. Sanchis, X. Roboam, and L. Marroyo, "Dynamic behavior of the doubly fed induction generator during three-phase voltage dips," *IEEE Trans. Energy Convers.*, vol. 22, no. 3, pp. 709–717, Sep. 2007.

[19] Z. Shuai, W. Huang, C. Shen, J. Ge, and Z. J. Shen, "Characteristics and restraining method of fast transient inrush fault currents in synchronverters," *IEEE Trans. Ind. Electron.*, vol. 64, no. 9, pp. 7487–7497, Sep. 2017.

[20] K. Shi, W. Song, P. Xu, R. Liu, Z. Fang, and Y. Ji, "Low-voltage ride-through control strategy for a virtual synchronous generator based on smooth switching," *IEEE Access*, vol. 6, pp. 2703–2711, 2018.

[21] C. Glöckler, D. Duckwitz, and F. Welck, "Virtual synchronous machine control with virtual resistor for enhanced short circuit capability," in *Proc. IEEE PES Innov. Smart Grid Technol. Conf. Europe*, 2017, pp. 1–6.

[22] H. Nian and Y. Jiao, "Improved virtual synchronous generator control of DFIG to ride-through symmetrical voltage fault," *IEEE Trans. Energy Convers.*, vol. 35, no. 2, pp. 672–683, Jun. 2020.

[23] S. Wang and L. Shang, "Fault ride through strategy of virtual-synchronous-controlled DFIG-based wind turbines under symmetrical grid faults," *IEEE Trans. Energy Convers.*, vol. 35, no. 3, pp. 1360–1371, Sep. 2020.

[24] A. Adib and B. Mirafzal, "Virtual inductance for stable operation of grid-interactive voltage source inverters," *IEEE Trans. Ind. Electron.*, vol. 66, no. 8, pp. 6002–6011, Aug. 2019.

[25] A. Rodríguez-Cabero, J. Roldán-Pérez, and M. Prodanovic, "Virtual impedance design considerations for virtual synchronous machines in weak grids," *IEEE J. Emerg. Sel. Topics Power Electron.*, vol. 8, no. 2, pp. 1477–1489, Jun. 2020.

[26] A. Adib, F. Fateh, and B. Mirafzal, "Smart inverter stability enhancement in weak grids using adaptive virtual-inductance," *IEEE Trans. Ind. Appl.*, vol. 57, no. 1, pp. 814–823, Jan./Feb. 2021.

[27] A. Gonzalez, E. J. Bueno, E. Saiz, A. Garcia, J. Aguilar, and J. L. Zamora, "Grid forming operation with a wound rotor induction generator," PCT application WO 2022/263331 A1, Jun. 2022.

[28] A. Yazdani and R. Iravani, *Voltage-Sourced Converters in Power Systems*. Hoboken, NJ, USA: Wiley, 2010.

[29] J. M. Uudrill, "Dynamic stability calculations for an arbitrary number of interconnected synchronous machines," *IEEE Trans. Power App. Syst.*, vol. PAS-87, no. 3, pp. 835–844, Mar. 1968.

[30] N. Pogaku, M. Prodanovic, and T. C. Green, "Modeling, analysis and testing of autonomous operation of an inverter-based microgrid," *IEEE Trans. Power Electron.*, vol. 22, no. 2, pp. 613–625, Mar. 2007.

[31] S.-D. Wee, M.-H. Shin, and D.-S. Hyun, "Stator-flux-oriented control of induction motor considering iron loss," *IEEE Trans. Ind. Electron.*, vol. 48, no. 3, pp. 602–608, Jun. 2001.

[32] X. Wang, Y. W. Li, F. Blaabjerg, and P. C. Loh, "Virtual-impedance-based control for voltage-source and current-source converters," *IEEE Trans. Power Electron.*, vol. 30, no. 12, pp. 7019–7037, Dec. 2015.

[33] J. Roldán-Pérez, A. Rodríguez-Cabero, and M. Prodanovic, "Design and analysis of virtual synchronous machines in inductive and resistive weak grids," *IEEE Trans. Energy Convers.*, vol. 34, no. 4, pp. 1818–1828, Dec. 2019.

[34] B. Wen, D. Boroyevich, R. Burgos, P. Mattavelli, and Z. Shen, "Analysis of D-Q small-signal impedance of grid-tied inverters," *IEEE Trans. Power Electron.*, vol. 31, no. 1, pp. 675–687, Jan. 2016.

[35] Y. Song, E. Ebrahimzadeh, and F. Blaabjerg, "Analysis of high-frequency resonance in DFIG-based offshore wind farm via long transmission cable," *IEEE Trans. Energy Convers.*, vol. 33, no. 3, pp. 1036–1046, Sep. 2018.

[36] Y. Gu, N. Bottrell, and T. C. Green, "Reduced-order models for representing converters in power system studies," *IEEE Trans. Power Electron.*, vol. 33, no. 4, pp. 3644–3654, Apr. 2018.

[37] X. Wang, L. Harnefors, and F. Blaabjerg, "Unified impedance model of grid-connected voltage-source converters," *IEEE Trans. Power Electron.*, vol. 33, no. 2, pp. 1775–1787, Feb. 2018.

[38] L. Harnefors, X. Wang, S.-F. Chou, M. Bongiorno, M. Hinkkanen, and M. Routimo, "Asymmetric complex-vector models with application to VSC–grid interaction," *IEEE Trans. Emerg. Sel. Topics Power Electron.*, vol. 8, no. 2, pp. 1911–1921, Jun. 2020.

[39] C. Zhang, X. Cai, A. Rygg, and M. Molinas, "Sequence domain SISO equivalent models of a grid-tied voltage source converter system for small-signal stability analysis," *IEEE Trans. Energy Convers.*, vol. 33, no. 2, pp. 741–749, Jun. 2018.

[40] A. Rygg, M. Molinas, C. Zhang, and X. Cai, "On the equivalence and impact on stability of impedance modeling of power electronic converters in different domains," *IEEE J. Emerg. Sel. Topics Power Electron.*, vol. 5, no. 4, pp. 1444–1454, Dec. 2017.

[41] J. Bao and P. L. Lee, *Process Control: The Passive Systems Approach*. Berlin, Germany: Springer, 2007.

[42] E. J. Bueno, S. Cobreces, F. J. Rodriguez, A. Hernandez, and F. Espinosa, "Design of a back-to-back NPC converter interface for wind turbines with squirrel-cage induction generator," *IEEE Trans. Energy Convers.*, vol. 23, no. 3, pp. 932–945, Sep. 2008.

Emilio José Bueno (Senior Member, IEEE) was born in Madrid, Spain, in 1972. He received the Ph.D. degree in electronics engineering from the University of Alcalá, Madrid, Spain, in 2005.

Since 2019, he has been a Full Professor with the Department of Electronics, University of Alcalá, and Cosupervisor of the Electronics Engineering Applied to the Renewable Energies Research Group. From 2010 to 2013, he was a Vice-Dean of the Polytechnic School, University of Alcalá, in charge of electrical engineering studies. His research interests include linear control of grid converters and drives, power quality, distributed generation systems, and medium-voltage converter topologies.

Javier Roldán-Pérez (Member, IEEE) received the B.S. degree in industrial engineering, the M.S. degree in electronics and control systems, the M.S. degree in system modeling, and the Ph.D. degree in power electronics all from Comillas Pontifical University, Madrid, Spain, in 2009, 2010, 2011, and 2015, respectively.

From 2010 to 2015, he was with the Institute for Research in Technology (IIT), Comillas University, Madrid. In 2014, he was a visiting Ph.D. student with the Department of Energy Technology, Aalborg University, Aalborg, Denmark. From 2015 to 2016, he was with the Electric and Control Systems Department, Norvento Energía Distribuida. In September 2016, he joined the Electrical Systems Unit, IMDEA Energy Institute, Madrid. In 2018, he did a research stay with SINTEF Energy Research, Trondheim, Norway. His research interests include renewable energies, microgrids, and power electronics applications.

Roberto Martín-López received the Electronics Communications Engineering degree and the M.Sc. degree in telecommunications in 2019 and 2021, respectively, from the University of Alcalá, Madrid, Spain, where he is currently working toward the Ph.D. degree in power electronics with the Department of Electronics in Electronics Engineering Applied to the Renewable Energies Research Group (GEISER), University of Alcalá, Madrid, Spain.

His research interests include power electronics, power control design, and SoC design applied to power electronics.

Elena Sáiz-Marín received the B.S. degree in industrial electrical engineering, and the Ph.D. degree in electrical power systems from Universidad Pontificia Comillas, Madrid, Spain, in 2010 and 2015, respectively.

Since 2016, she has been working on developing projects related with massive renewable generation integration focusing on wind turbines.

Adrián González-Cajigas (Student Member, IEEE) received the M.Sc. degree in electronic systems engineering from Carlos III University, Leganés, Spain, in 2018. He is currently working toward the Ph.D. degree in power electronics with the University of Alcalá, Madrid, Spain.

From 2018 to 2022, he was a Member of the Electronics Engineering Applied to Renewable Energies Research Group (GEISER) with University of Alcalá. He is currently with Siemens Gamesa, Madrid. His research interests include control of voltage-source converters applied to renewable energy, distributed generation systems, and parallel converters operation.